Rare Met.
https://doi.org/10.1007/s12598-xxx-xxxxx-x

RARE METALS

Original Article

Oxidation sequence modulation induced superior high-temperature tribological performance of the Ti-Hf-Nb-V refractory high entropy alloy fabricated through directed energy deposition

Yong-Yun ZHANG, Cong-Rui Yang, Xing Tong, Jing Zhou, Lin Liu, Meng Xiao, Hai-Bo Ke *(iD 0000-0003-3657-0403), Kang-Cheung Chan *(iD 0000-0002-6173-5532), Wei-Hua Wang *(iD 0000-0002-9155-2462)

Received:*** / Revised: *** / Accepted: ***

Abstract To fulfill the demands of applications under severe operational conditions, alloys should possess outstanding wear resistance at elevated temperatures. A Ti-Hf-Nb-V based refractory high entropy alloy (RHEA) was successfully produced using the directed energy deposition (DED) technique, which avoided the formation of fatal defects and showcased well-performed mechanical properties across a broad temperature spectrum. Strategic design of the oxidation sequence enabled the early formation of oxide nanolayers, which can form a polycrystalline oxide nanocoating under a complex stress condition to drastically reduce the wear rate from 2.69×10^{-4} $mm^3 \cdot (N \cdot m)^{-1}$ at room temperature to 6.90×10^{-7} $mm^3 \cdot (N \cdot m)^{-1}$ at 600 °C. These results indicate that the application of additive manufacturing (AM) to fabricate RHEAs with superior wear resistance at high temperatures paves the way for the development of functional coatings designed to withstand extreme conditions.

Keywords Refractory high entropy alloy; directed energy deposition; high temperature; wear resistance; Oxidation sequence design

Supplementary Information The online version contains supplementary material available at…

Y.-Y. Zhang, C.-R. Yang, X. Tong, J. Zhou, H.-B. Ke*, W.-H. Wang*
Songshan Lake Materials Laboratory, Dongguan 523808, China
e-mail: kehaibo@sslab.org.cn; whw@iphy.ac.cn

Y.-Y. Zhang, C.-R. Yang, K.-C. Chan*
Research Institute for Advanced Manufacturing, Department of Industrial and Systems Engineering, The Hong Kong Polytechnic University, Hong Kong 999077, China
e-mail: kc.chan@polyu.edu.hk

L. Lin
State Key Laboratory of Material Processing and Die & Mould Technology and School of Materials Science and Engineering, Huazhong University of Science and Technology, Wuhan 430074, China

M. Xiao
School of Chemistry and Materials Science, Guangdong University of Education, Guangzhou 510640 China

1 Introduction

Most mechanical component failures are caused by surface wear, with significant cost implications [1]. Therefore, developing materials with excellent wear resistance is a major focus for researchers [2,3]. Refractory high entropy alloys (RHEAs) are promising for high-temperature applications due to their superior properties [4–6]. However, RHEAs tend to be brittle at room temperature (RT) [7], making them vulnerable to fatigue wear [8], resulting in poor wear resistance [9]. This presents a key issue and technical challenge that needs to be addressed urgently. The laser-aided directed energy deposition (DED) technique, characterized by its integrated design and manufacturing approach, high processing precision and short manufacturing cycle [10], can produce RHEA deposits with superior strength and hardness, mainly attributed to solid solution strengthening [10] or grain refinement [11,12]. In general, the preparation of high-quality deposits with high hardness, plastic toughness, and minimal defects significantly improves wear resistance [13,14]. Although the formation of precipitation can increase the hardness of RHEAs [15,16], blindly increasing the content of the precipitated phases cannot significantly improve the material's wear resistance [17]. In previous research, a $Ti_{42}Hf_{21}Nb_{21}V_{16}$ (T42) RHEA prepared by laser-engineered net shaping (LENS) had better plasticity than the same type of RHEA prepared by casting [10], which may enable its favorable friction and wear properties. As prospective high-temperature engineering materials, the wear resistance of RHEAs is volatile and readily affected by ambient temperatures [18–20]. Although adjusting the fabrication parameters seems to work on improving the high-temperature tribological performance of fabricated RHEA deposits, like applying ultrasonic vibration [12], changing laser power [21] and applying a remelting approach [22], forming a denser glaze on the wear surface would be more productive for improving the tribological properties at elevated temperatures [23,24]. As a result, how to regulate the formation of high-temperature oxidation products to modify the tribological properties of RHEAs becomes of great significance to the preparation of highly applicable HEA deposits.

In this study, we used the LENS method to fabricate the T42 RHEA deposit, which demonstrated superior tensile strength, ductility, and wear resistance at elevated temperatures. By controlling oxidation product formation, we significantly improved wear performance from RT to 600 °C. Additionally, we explored the wear mechanisms of LENS-fabricated RHEAs at high temperatures, offering new insights into creating RHEAs with enhanced properties for extreme conditions.

2 Experimental

High-purity elemental powder blends were used as the starting materials in our LENS process, with the detailed fabrication parameters given in Ref [10]. The alloy was used to make test specimens via electrical wire-cutting, prepared for various experiments. Phase analysis was done using X-ray diffraction (XRD, Mo, λ = 0.71 Å), and specimens were polished using a series of techniques before electron backscatter diffraction (EBSD, C-swift). An aberration-corrected transmission electron microscope (TEM, Spectra 300) with selected area electron diffraction (SAED) was used for microstructural characterization. The microhardness of RHEA was measured with a Vickers Hardness tester, and nanoindentation tests (Bruker Ti980), applying a 100 mN load with a 15 s dwell time, assessed nano-hardness and elastic modulus. Tensile yield strength was measured at various temperatures using a ZwickRoell machine with a heating chamber (details in Ref. [25]). Tribological properties were evaluated at different temperatures using a ball-on-disk tribometer (MFT-5000, RTEC Instruments) with an Al_2O_3 ball (diameter of 9.53 mm), and the coefficient of friction (COF) was monitored in real time. Wear tests were conducted at RT, 400, 500, 600, 700 and 800 ℃, with a 10 N normal load, a 2 mm stroke length, a 5 Hz reciprocating frequency, and a 30-minute duration. The post-wear analysis involved a 3D Optical Profiler (S Neox) and scanning electron microscopy (SEM, Verios 5UC) with energy-dispersive spectroscopy (EDS, X-max 80) to study the worn surfaces. TEM (Talos F200X) with EDS, aided by a focused ion beam (FIB, Helios 5 UX), characterized subsurface morphologies. High-temperature oxidation behavior was assessed by oxidation tests at 600 and 800 ℃ for 12 h, with the mass gain tracked over time, with post-oxidation XRD (Cu, λ = 1.54 Å), SEM, and EDS analyses to examine phase changes and elemental distributions.

3 Results

To investigate the microstructure and phase composition of the T42 RHEA, we used various characterization techniques. XRD patterns (**Fig. 1**a) revealed a single body-centered cubic (BCC) phase after the LENS process. Surface microstructure analysis (**Fig. 1**b(i)) showed equiaxed grains and confirmed the single BCC phase (**Fig. 1**b(ii)). At the nanoscale (**Fig. 1**c), contrast variations indicated lattice distortions, but the SAED patterns confirmed the BCC structure. Hardness assessments showed an average microhardness of 367 ± 3.4 $HV_{0.2}$. Nanoindentation tests (**Fig. 1**d) indicated a smooth load vs. depth curve with no pop-in phenomena, yielding a hardness of 4.40 ± 0.06 GPa and an elastic modulus of 107 ± 0.87 GPa. Yield strength measurements (**Fig. 1**e) demonstrated that the alloy maintains gigapascal-level strength at RT, decreasing to 630-680 MPa at higher temperatures, with details given in our previous study [25].

We performed reciprocating dry friction tests at various temperatures (typically RT, 400, 600 and 800 ℃) on the fabricated alloy. **Figure S1** (in Supplementary Information (SI)) shows the COF curves as a function of sliding duration under different thermal conditions. The average COFs vary from 0.4 to 0.5 for temperatures below 800 °C, while at 800 °C, the COF drops to approximately 0.28. Notably, at 800 °C, the COF is significantly lower, but its temporal stability shows more fluctuations compared to those at lower temperatures. **Fig. 2**a shows the 3D profiles of the wear scars on the RHEAs after grinding against Al_2O_3 balls at varying temperatures. **Fig. 2**b provides 2D profiles of the central area of the wear scars along the cross-section. As the temperature rises from RT to 400 °C, the width of the wear scar decreases by approximately 19%, from 2285 μm at RT to 1860 μm at 400 °C, while the maximum depths remain around 41 μm. The formation of ridges around the wear scars suggests that the RHEA tends to extrude laterally during the dry sliding wear tests, indicating the alloy's good plastic deformation capability. At 600 °C, the wear scar's width and depth significantly decrease, with the maximum wear depth falling below 1 μm. The wear volumes for each sample were determined from the 3D profiles of the worn surfaces, and the wear rate (ω) was calculated using the following equation [26]:

$$\omega = V/(L \times F) \quad (1)$$

where V corresponds to the wear volume (mm^3), L denotes the total sliding distance (m), and F refers to the applied normal load (N). **Fig. 2**c shows the wear rates as a function of temperature, indicating a decrease in wear rate from RT to 600 °C. At RT, the wear rate of the RHEA is approximately 2.69×10^{-4} $mm^3 \cdot (N \cdot m)^{-1}$, while at 600 °C, it is nearly three orders of magnitude lower, at about 6.90×10^{-7} $mm^3 \cdot (N \cdot m)^{-1}$. The wear rate increases to 3.10×10^{-5} $mm^3 \cdot (N \cdot m)^{-1}$ when the temperature rises to 800 ℃. For the samples tested at 500 and 700 ℃, with the wear scars given in **Figure S2**, higher wear rates were also formed compared to the sample tested at 600 ℃, indicating that the RHEA has optimal wear resistance around 600 °C. **Fig. 2**d compares the tribological performance of our RHEA with other reported RHEAs [9,18–20,27,28], showing that our designed RHEA demonstrates exceptional wear resistance at high temperatures, particularly around 600 °C.

We examined the worn surfaces of the fabricated RHEA and the Al_2O_3 sliding ball after dry friction tests to understand the wear mechanisms. **Figure S3** a captures the 3D morphology of the wear region on the Al_2O_3 ball surface after interaction with the RHEA under different thermal conditions. At RT and 400 °C, the ball surface wear is characterized by distinct circular planes, whereas, at higher temperatures, the wear is less pronounced. The corresponding SEM and EDS images indicate detachment of Al_2O_3 grains along their boundaries at RT and 400 °C, while the EDS results show the presence of alloy elements (Ti, Hf, Nb, V, and O) mixed with Al_2O_3 (as shown in **Figure S3**), suggesting the presence of adhesive wear. Further analysis of the RHEA's worn surfaces, as shown in **Fig. 3**, reveals different wear mechanisms at various temperatures. At RT, severe abrasive wear is indicated by the abundant wear debris and deep grooves, while the same similar wear features with significant plastic deformation suggest a combination of abrasive wear and plastic deformation at 400 °C. As the temperature increases to 600 °C, a smoother surface with an oxide layer indicates a transition to oxidative wear. The surface remains relatively smooth, but the formation of various oxides (Hf, Nb, and their oxides) degrades wear performance, increasing the wear rate at the temperature of 800 °C.

We examined the cross-sectional morphologies of the wear tracks on the fabricated RHEA. At temperatures from RT to 400 °C (**Figure S4** a, b), a distinct friction layer forms from the compacted wear debris [26,29]. At RT, this layer shows cracks that likely lead to its disintegration and accelerated wear. At 400 °C, the friction layer is similar but without cracks, suggesting enhanced wear resistance. When the temperature increases to 600 °C (**Figure S4**c), the worn surface is smoother and lacks a thick oxidation layer. Bulk oxides form within the matrix at 800 °C (**Figure S4**d), with internal cracks that exacerbate wear. To investigate deformation and oxidation post-dry friction tests at various temperatures, we used FIB and TEM on the worn scars from the RT and 600 °C tests. **Figure S5**a shows the FIB sampling area. At RT, reciprocating sliding induces plastic deformation beneath the wear scar (**Figure S5**b), forming nano-grains that increase in size with depth (**Figure S5**c). The SAED pattern confirms the nano-sized grains as the single BCC phase of the RHEA matrix (**Figure S5**c (iii)), and high resolution transmission electron microscope (HRTEM) image supports the formation of these grains (**Figure S5**c (iv)). EDS analysis (**Figure S5**d) reveals an even elemental distribution without extensive oxide formation post-RT test. We focused on studying the cross-sectional microstructure of the 600 °C test sample, which has a dramatically low wear rate. **Fig. 4**a shows the TEM sampling area with a flattened worn surface and distinct oxide layers. TEM images reveal a stratified structure with a high dislocation density beneath the surface (**Fig. 4**b). The magnified image (**Fig. 4**c) shows clear layer boundaries and an oxygen gradient, with more oxygen at the top and diminishing levels towards the bottom. Further analysis of the phase composition of different layers beneath the wear surface is provided by the SAED patterns and HRTEM atomic maps (**Fig. 4**d). While the upper layer under the wear surface is confirmed to have nano-sized grains, the lattice constant differs from the BCC matrix shown in **Figure S5**. The bottom layer maintains a single BCC structure, as evidenced by the atomic structure in **Fig. 4**d, whereas the middle layer appears to have a distorted lattice and is identified as HfO_2. For the upper layer, nanocrystals of a mixture between TiO_2 and HfO_2 were formed in the ultra-thin film based on the SAED pattern, with a thickness of ~ 200 nm.

The wear rate reduction observed at 600 °C compared to 800 °C (**Fig. 2**c) suggests enhanced wear resistance, likely due to different oxidation behavior at these temperatures. Static oxidation experiments were conducted to investigate this phenomenon. **Fig. 5**a shows the mass gains of the RHEA at varying temperatures over time, with a sharper increase at 800 °C compared to 600 °C, indicating faster oxide formation at higher temperatures. The Gibbs free energy change (ΔG) curves (**Fig. 5**b) indicate that Ti and Hf elements in the alloy have significantly lower ΔG to form their oxides compared to other elements, favoring their initial oxidation at high temperatures. XRD analysis (**Fig. 5**c) revealed the initial formation of TiO_2 or HfO_2 alongside a predominantly BCC matrix at 600 °C, with lattice expansion indicating oxygen absorption. At 800 °C (**Fig. 5**d), diverse oxides formed initially, with minimal change upon prolonged exposure. Morphological analysis (**Fig. 5** d, e) highlighted distinct oxidation behavior: noticeable Nb, Ti, Hf, and V oxides formed at higher temperatures, evident from elemental distribution maps.

4 Discussion

The empirical model by Archard [14] proposes a wear rate inversely related to yield strength or hardness. However, the as-fabricated RHEA exhibits better wear resistance at 600 °C than at RT (**Fig. 2**c), challenging this model in the counter-grinding system. Adhesive wear and material transfer occur due to high shear stress at the adhesive nodes during dry sliding friction at RT and 400 °C (**Figure S3**), influencing the wear dynamics. Below 600 °C, elastic collision effects with Al_2O_3 and the peeling of Al_2O_3 particles contribute to the wear process, leading to a randomly distributed adhesive layer (**Figure S3** a, b) and poor wear resistance (**Fig. 2**c). Additionally, strip-shaped grooves along the sliding direction (**Fig. 3** a, b) were produced due to micro-cutting and plastic deformation under frictional forces and normal loads [30], influenced by the

alloy's overall mechanical properties. As a result, we then considered the influence of elastic moduli in calculating the maximum contact stress (P_{max}) using Hertzian contact mechanics [31], with details shown in **Note 2** (SI). Values of P_{max}, ranging from 910 to 980 MPa under a 10 N static load, listed in **Table S2**, exceed the yield strength of the RHEA at elevated temperatures (**Fig. 1**), resulting in plastic deformation during the RT and high-temperature tribological processes (**Figure S5**).

The formation and composition of oxides play a crucial role in high-temperature tribological behavior, significantly influenced by the environmental temperature [32]. At elevated temperatures and under mechanical stress, RHEAs undergo complex physical and chemical transformations [20,26], including micro-protrusion adhesion, surface material spalling, subsurface micro-defect initiation and growth, surface oxidation, and oxide layer formation and detachment. As the temperature rises, a transition to oxidative wear occurs. Friction under high contact pressure induces plastic deformation (**Figure S5**), facilitating oxygen atom diffusion into the metal matrix [33] and forming a protective oxide layer [26]. This oxide layer is typically harder than the substrate, providing wear protection [34,35]. Certain metal oxides can act as dry friction lubricants at high temperatures [26,36], reducing direct friction pair contact, and thereby lowering the friction coefficient and wear rate [36].

Under further oxidative wear conditions, the wear rate depends on oxidation film thickness and oxide quantity [37]. The high-temperature oxidation behavior of the fabricated RHEA, composed of multiple components, is complex and governed by both kinetic and thermodynamic factors [38,39]. Initially, Ti and Hf, with lower ΔG values (**Fig. 5**b), are preferentially oxidized, and the sluggish diffusion in HEAs [39] prevents internal elements from replenishing the surface, leading to a compositional gradient (**Fig. 4**c). At this stage, a mixed oxide of TiO_2 and HfO_2 forms, resulting in the rapid initial weight gain (Fig. 5a) and impeding the diffusion of O_2 from air, thus protecting the alloy from severe oxidation [40]. In addition, the oxide layer needs strong matrix support to effectively reduce wear [41]. Hence, we introduced the Pilling-Bedworth ratio ($R_{P\text{-}B}$), which can be used to assess the degree of oxide expansion during growth [42,43], to evaluate the bonding strength between the oxidation layer and substrate [44], defined as:

$$R_{P-B} = V_o/(n \cdot V_m) = M_o \cdot \rho_m/(n \cdot M_m \cdot \rho_o) \quad (2)$$

This ratio compares the oxide film volume (V_O) to the consumed metal volume (V_m) by using the relative molecular/atomic masses of the oxide (M_O) and metal (M_m), their densities (ρ_m and ρ_O) and the number of metal atoms per oxide molecule (n). The calculated $R_{P\text{-}B}$ values of different oxidation products are given as follows: HfO_2 (1.592), TiO_2 (1.777), Nb_2O_5 (2.665), and V_2O_5 (3.240). A $R_{P\text{-}B}$ value between 1 and 2 indicates good adhesion and protection against oxidation [45], while a value over 2 suggests that the oxide is prone to expansion, cracking, and is relatively loose, failing to offer adequate protection [46]. The initially formed TiO_2 and HfO_2 oxides, with $R_{P\text{-}B}$ values close to 1-2, indicate good adhesion [42,43]. Additionally, the proliferation of ultra-thin TiO_2 and HfO_2 oxide nanocrystal layer on the subsurface of RHEA ground at 600 °C (**Fig. 4**c), impedes further oxidation [40] and contributes to reduced wear rates [26]. This is why a superior resistance of the fabricated alloy was produced at 600 ℃ in this study.

As the temperature increases to 800 °C, internal oxidation occurs with extensive alloying element segregation, disrupting the oxide film structure, precipitating various oxides (**Fig. 5**e), forming different oxidation products (**Fig. 5**c), and increasing the oxidation weight gains (**Fig. 5**a). Under cyclic loading, cracks propagate within the matrix (**Figure S4**d), exposing it to atmospheric oxygen, and forming double or multi-layered oxide structures (**Figure S4**d). Internal oxides alter the crack stress field, accelerating their expansion [47]. When the cracks reach critical sizes, matrix portions detach with upper oxide layers, generating large wear debris observed on the grinding ball **Fig. 2**a), perpetuating oxidative wear cycles [48], and resulting in worsened wear resistance compared to samples ground at 600 °C. In summary, by designing the oxidation sequence, remarkable wear resistance under high temperatures was achieved in our fabricated RHEA.

5 Conclusion

In this study, a Ti-Hf-Nb-V based RHEA was synthesized via LENS, focusing on its microstructure, tribological properties, and oxidation behavior at various temperatures. The T42 RHEA, fabricated with LENS, exhibited a single-phase bcc structure with uniform element distribution, maintaining high yield strength at RT and elevated temperatures. Wear resistance significantly improved at 600 °C compared to other temperatures by strategically controlling the oxidation sequence to pre-form the TiO_2 and HfO_2 layers. This nanocrystalline coating with good bonding strength with substrate reduced the wear rate to 6.90×10^{-7} $mm^3 \cdot (N \cdot m)^{-1}$, a nearly three-order decrease compared to that at RT. At 800 °C, diverse oxidation products with large expansion degrees formed a brittle, loosely structured oxidation film prone to cracking and detachment under frictional stress, lowering the COF but adversely affecting the wear resistance.

Acknowledgments This work was financially supported by Guangdong Major Project of Basic and Applied Basic Research, China (No. 2019B030302010), the joint research scheme of National Natural Science Foundation of China (NSFC) and Research Grants Council of Hong Kong (RGC) (Nos. 52061160483 and N_PolyU523/20), the National Natural Science Foundation of China (Nos. 52104362, 52071222, 52471179, 52471180 and 52001221), the National Key R&D Program of China (No. 2022YFA1603800), the National Key

Research and Development Program of China (No. 2021YFA0716302), Guangdong Provincial Quantum Science Strategic Initiative (No. GDZX2301001) and Guangdong Basic and Applied Basic Research, China (No. 2020B1515130007).

Declarations

Conflict of interests The authors declare that they have no conflict of interest.

References

[1] Gagg, C.R., Lewis, P.R., Wear as a product failure mechanism - Overview and case studies, Eng. Fail. Anal. 2007; 14 (8) : 1618. https://doi.org/10.1016/j.engfailanal.2006.11.064.
[2] Zhai, W., Bai, L., Zhou, R., Fan, X., Kang, G., Liu, Y., Zhou, K., Recent Progress on Wear-Resistant Materials: Designs, Properties, and Applications, Adv. Sci. 2021; 8 (11) : 1. https://doi.org/10.1002/advs.202003739.
[3] Bai, H., Zhong, L., Kang, L., Liu, J., Zhuang, W., Lv, Z., Xu, Y., A review on wear-resistant coating with high hardness and high toughness on the surface of titanium alloy, J. Alloys Compd. 2021; 882 : 160645. https://doi.org/10.1016/j.jallcom.2021.160645.
[4] Senkov, O.N., Miracle, D.B., Chaput, K.J., Couzinie, J.P., Development and exploration of refractory high entropy alloys - A review, J. Mater. Res. 2018; 33 (19) : 3092. https://doi.org/10.1557/jmr.2018.153.
[5] Zhang, W.-T., Wang, X.-Q., Zhang, F.-Q., Cui, X.-Y., Fan, B.-B., Guo, J.-M., Guo, Z.-M., Huang, R., Huang, W., Li, X.-B., others, Frontiers in high entropy alloys and high entropy functional materials, Rare Met. 2024; 43 (10) : 4639. https://doi.org/doi.org/10.1007/s12598-024-02852-0.
[6] Ying, H.-Q., Liu, S.-N., Wu, Z.-D., Dong, W.-X., Ge, J.-C., Hahn, H., Provenzano, V., Wang, X.-L., Lan, S., Phase selection rule of high-entropy metallic glasses with different short-to-medium-range orders, Rare Met. 2022; 41 (6) : 2021. https://doi.org/10.1007/s12598-022-01973-8.
[7] Xiong, W., Guo, A.X.Y., Zhan, S., Liu, C.T., Cao, S.C., Refractory high-entropy alloys: A focused review of preparation methods and properties, J. Mater. Sci. Technol. 2023; 142 : 196. https://doi.org/10.1016/j.jmst.2022.08.046.
[8] Ritchie, R.O., Mechanisms of fatigue-crack propagation in ductile and brittle solids, Int. Joournal Fract. 1999; 100 (1) : 55. https://doi.org/10.1088/1009-0630/14/2/06.
[9] Pole, M., Sadeghilaridjani, M., Shittu, J., Ayyagari, A., Mukherjee, S., High temperature wear behavior of refractory high entropy alloys based on 4-5-6 elemental palette, J. Alloys Compd. 2020; 843 : 156004. https://doi.org/10.1016/j.jallcom.2020.156004.
[10] Zhang, Y., Qin, B., Ouyang, D., Liu, L., Feng, C., Yan, Y., Ye, S., Ke, H., Chan, K.C., Wang, W., Strong yet ductile refractory high entropy alloy fabricated via additive manufacturing, Addit. Manuf. 2024; 81 : 104009. https://doi.org/10.1016/j.addma.2024.104009.
[11] Chen, L., Zhang, X., Wang, Y., Hao, X., Liu, H., Microstructure and elastic constants of AlTiVMoNb refractory high-entropy alloy coating on Ti6Al4V by laser cladding, Mater. Res. Express 2019; 6 (11) : 116571. https://doi.org/10.1088/2053-1591/ab49e7.
[12] Zhao, Y., Wu, M., Hou, J., Chen, Y., Zhang, C., Cheng, J., Li, R., Microstructure and high temperature properties of laser cladded WTaNbMo refractory high entropy alloy coating assisted with ultrasound vibration, J. Alloys Compd. 2022; 920 : 165888. https://doi.org/10.1016/j.jallcom.2022.165888.
[13] Lu, K., Zhu, J., Guo, D., Yang, M., Sun, H., Wang, Z., Hui, X., Wu, Y., Microstructures, Corrosion Resistance and Wear Resistance of High-Entropy Alloys Coatings with Various Compositions Prepared by Laser Cladding: A Review, Coatings 2022; 12 (7) : 1023. https://doi.org/10.3390/coatings12071023.
[14] Archard, J.F., Contact and rubbing of flat surfaces, J. Appl. Phys. 1953; 24 (8) : 981. https://doi.org/10.1063/1.1721448.
[15] Wang, H., Liu, Q., Guo, Y., Lan, H., $MoFe_{1.5}CrTiWAlNb_x$ refractory high-entropy alloy coating fabricated by laser cladding, Intermetallics 2019; 115 : 1. https://doi.org/10.1016/j.intermet.2019.106613.
[16] Li, Q., Zhang, H., Li, D., Chen, Z., Huang, S., Lu, Z., Yan, H., $W_xNbMoTa$ refractory high-entropy alloys fabricated by laser cladding deposition, Materials (Basel). 2019; 12 (3) : 1. https://doi.org/10.3390/ma12030533.
[17] Guo, Y., Li, X., Liu, Q., A novel biomedical high-entropy alloy and its laser-clad coating designed by a cluster-plus-glue-atom model, Mater. Des. 2020; 196 : 109085. https://doi.org/10.1016/j.matdes.2020.109085.
[18] Jin, C., Li, X., Li, H., Li, Q., Wang, H., Tribological performance of a $TiZrNbMo_{0.6}$ refractory high entropy alloy at elevated temperatures, J. Alloys Compd. 2022; 920 : 165915. https://doi.org/10.1016/j.jallcom.2022.165915.
[19] Pei, X., Du, Y., Hao, X., Wang, H., Zhou, Q., Wu, H., Wang, H., Microstructure and tribological properties of $TiZrV_{0.5}Nb_{0.5}Al_x$ refractory high entropy alloys at elevated temperature, Wear 2022; 488–489 : 204166. https://doi.org/10.1016/j.wear.2021.204166.
[20] You, X., Song, J., Lin, P., Zhang, X., Su, Y., Wang, H., Zhang, Y., Hu, L., Tribological properties and wear mechanisms of $Ti_xVNbTaW_y$ RHEAs sliding against Si_3N_4 ceramic balls: The effects of Ti and W contents, Tribol. Int. 2022; 175 : 107801. https://doi.org/10.1016/j.triboint.2022.107801.
[21] Liu, X., Liu, Y., Guo, W., Feng, K., Zhu, K., Zhang, Z., Zhang, F., Chai, L., Guo, N., Guo, S., Influence of laser power on microstructure and high-temperature tribological properties of CoAlTiWTa RHEA coating on Inconel 718 superalloy, Surf. Coatings Technol. 2024; 479 : 130573. https://doi.org/10.1016/j.surfcoat.2024.130573.
[22] Sun, B., Wang, Q., Chen, Y., Wang, B., Xia, M., Gu, T., Zhu, S., Zhang, B., Liang, X., Shen, B., Design of heterogeneous structure for enhancing formation quality of laser-manufactured WTaMoNb refractory high-entropy alloy, J. Alloys Compd. 2023; 953 : 170066. https://doi.org/10.1016/j.jallcom.2023.170066.
[23] Joseph, J., Haghdadi, N., Shamlaye, K., Hodgson, P., Barnett, M., Fabijanic, D., The sliding wear behaviour of CoCrFeMnNi and $Al_xCoCrFeNi$ high entropy alloys at elevated temperatures, Wear 2019; 428–429 : 32. https://doi.org/10.1016/j.wear.2019.03.002.
[24] Löbel, M., Lindner, T., Pippig, R., Lampke, T., High-temperature wear behaviour of spark plasma sintered $AlCoCrFeNiTi_{0.5}$ high-entropy alloy, Entropy 2019; 21 (6) : 582. https://doi.org/https://doi.org/10.1016/j.msea.2024.147225.
[25] Zhang, Y., Yu, K., Qin, B., Yang, C., Ye, S., Feng, C., Zhang, F., Ouyang, D., Liu, L., Ke, H., others, Origins of strength stabilities at elevated temperatures in additively manufactured refractory high entropy alloy, Mater. Sci. Eng. A 2024; 915 : 147225.
[26] Li, H., Li, X., Jin, C., Li, Q., Ma, Q., Hua, K., Wang, H., Liu, W., Mechanical and tribological performance of $AlCr_{0.5}NbTa_xTi_{4-x}$ (x = 0, 0.5, 1) refractory high-entropy alloys, J. Mater. Sci. Technol. 2023; 156 : 241. https://doi.org/10.1016/j.jmst.2023.02.016.
[27] Mengis, L., Grimme, C., Galetz, M.C., Tribological properties of the uncoated and aluminized Ti–48Al–2Cr–2Nb TiAl alloy at high temperatures, Wear 2021; 477 : 203818. https://doi.org/10.1016/j.wear.2021.203818.
[28] Alvi, S., Akhtar, F., High temperature tribology of CuMoTaWV high entropy alloy, Wear 2019; 426–427 : 412. https://doi.org/10.1016/j.wear.2018.12.085.
[29] Nguyen, C., Tieu, A.K., Deng, G., Wexler, D., Tran, B., Vo, T.D., Study of wear and friction properties of a Co-free $CrFeNiAl_{0.4}Ti_{0.2}$ high entropy alloy from 600 to 950 °C, Tribol. Int. 2022; 169 : 107453. https://doi.org/10.1016/j.triboint.2022.107453.
[30] Vakis, A.I., Yastrebov, V.A., Scheibert, J., Nicola, L., Minfray, C., Almqvist, A., Paggi, M., Lee, S., Molinari, J.F., Anciaux, G., Restrepo, S.E., Papangelo, A., Nicolini, P., Aghababei, R., Putignano, C., Stupkiewicz, S., Lengiewicz, J., Costagliola, G., Bosia, F., Guarino, R., Pugno, N.M., Dini, D., Müser, M.H., Ciavarella, M., Models and Methods for Tribology Across Scales : an Overview, Tribol. Int. 2018; 125 : 169. https://doi.org/https://doi.org/10.1016/j.triboint.2018.02.005.
[31] Hutchings, I., Shipway, P., Tribology: Friction and Wear of Engineering Materials, Second Edi, Butterworth-Heinemann; 2017.
[32] Wang, S.Q., Wang, L., Zhao, Y.T., Sun, Y., Yang, Z.R., Mild-to-severe wear transition and transition region of oxidative wear in steels, Wear 2013; 306 (1–2) : 311. https://doi.org/10.1016/j.wear.2012.08.017.
[33] Wang, X., Mao, D., Wei, X., Li, J., Meng, H., Wang, W., Sliding friction induced atom diffusion in the deformation layer of 0.45% C steel rubbed against Tin alloy, Tribol. Int. 2013; 64 : 128. https://doi.org/10.1016/j.triboint.2013.03.008.
[34] An, X.L., Liu, Z.D., Zhang, L.T., Zou, Y., Xu, X.J., Chu, C.L., Wei, W., Sun, W.W., A new strong pearlitic multi-principal element alloy to withstand wear at elevated temperatures, Acta Mater. 2022; 227 : 117700.

https://doi.org/10.1016/j.actamat.2022.117700.
[35] Feng, K., Shao, T., The evolution mechanism of tribo-oxide layer during high temperature dry sliding wear for nickel-based superalloy, Wear 2021; 476 : 203747. https://doi.org/10.1016/j.wear.2021.203747.
[36] Hsu, S.M., Shen, M.C., Ruff, A.W., Wear prediction for metals, Tribol. Int. 1997; 30 (5) : 377. https://doi.org/https://doi.org/10.1016/S0301-679X(96)00067-9.
[37] Lim, S.C., The relevance of wear-mechanism maps to mild-oxidational wear, Tribol. Int. 2002; 35 (11) : 717. https://doi.org/10.1016/S0301-679X(02)00033-6.
[38] Jayaraj, J., Thirathipviwat, P., Han, J., Gebert, A., Microstructure, mechanical and thermal oxidation behavior of AlNbTiZr high entropy alloy, Intermetallics 2018; 100 : 9. https://doi.org/10.1016/j.intermet.2018.05.015.
[39] Ouyang, D., Chen, Z. jie, Yu, H. bin, Chan, K.C., Liu, L., Oxidation behavior of the $Ti_{38}V_{15}Nb_{23}Hf_{24}$ refractory high-entropy alloy at elevated temperatures, Corros. Sci. 2022; 198 : 110153. https://doi.org/10.1016/j.corsci.2022.110153.
[40] Kumar, P., Lam, T.N., Tripathi, P.K., Singh, S.S., Liaw, P.K., Huang, E.W., Recent progress in oxidation behavior of high-entropy alloys: A review, APL Mater. 2022; 10 : 120701. https://doi.org/10.1063/5.0116605.
[41] Kato, H., Severe-mild wear transition by supply of oxide particles on sliding surface, Wear 2003; 255 : 426. https://doi.org/10.1016/S0043-1648(03)00077-2.
[42] Pilling, N., Bedworth, R., The oxidation of metals at high temperatures, Inst. Met. 1923; 29 : 529. https://cir.nii.ac.jp/crid/1571698600147960192
[43] Xu, C., Gao, W., Pilling-Bedworth ratio for oxidation of alloys, Mater. Res. Innov. 2000; 3 (4) : 231. https://doi.org/https://doi.org/10.1007/s100190050008.
[44] Jarvis, E.A.A., Carter, E.A., Exploiting covalency to enhance metal–oxide and oxide–oxide adhesion at heterogeneous interfaces, J. Am. Ceram. Soc. 2003; 86 (3) : 373. https://doi.org/https://doi.org/10.1111/j.1151-2916.2003.tb03309.x.
[45] Jiang, Q., Lu, D., Liu, C., Liu, N., Hou, B., The Pilling-Bedworth Ratio of Oxides Formed From the Precipitated Phases in Magnesium Alloys, Front. Mater. 2021; 8 : 761052. https://doi.org/10.3389/fmats.2021.761052.
[46] Tan, Q., Atrens, A., Mo, N., Zhang, M.X., Oxidation of magnesium alloys at elevated temperatures in air: A review, Corros. Sci. 2016; 112 : 734. https://doi.org/10.1016/j.corsci.2016.06.018.
[47] Hancock, P., Hurst, R.C., The Mechanical Properties and Breakdown of Surface Oxide Films at Elevated Temperatures, in: M.G. Fontana, R.W. Staehle (Eds.), Adv. Corros. Sci. Technol. Vol. 4, Boston, MA: Springer US; 1974. pp. 1. https://doi.org/10.1007/978-1-4615-9059-0_1.
[48] So, H., The mechanism of oxidational wear, Wear 1995; 184 (2) : 161. https://doi.org/https://doi.org/10.1016/0043-1648(94)06569-1.

氧化序列调控对定向能量沉积制备的 Ti-Hf-Nb-V 难熔高熵合金高温摩擦学性能的增强作用研究

张永赟，杨丛瑞，童星，周靖，柯海波*，汪卫华*
松山湖材料实验室，东莞，523808，中国
邮箱：kehaibo@sslab.org.cn；whw@iphy.ac.cn

张永赟，杨丛瑞，陈镜昌*
工业及系统工程学系，香港理工大学，香港， 999077，中国
邮箱：kc.chan@polyu.edu.hk

柳林
材料科学与工程学院，华中科技大学，武汉，430074，中国

肖猛
化学与材料科学学院，广东第二师范学院，广州，510640，中国

摘要 (Chinese Abstract)
为了满足严苛条件下的应用需求，合金通常需具备优异的高温耐磨性能。通过定向能量沉积技术制备的 Ti-Hf-Nb-V 难熔高熵合金，没有行程致命的缺陷，并在大的温度范围内表现出良好的机械性能。通过设计该合金中的氧化顺序，在摩擦磨损实验中可以行程氧化物的纳米层。在 600℃下，该氧化物纳米层的形成，能够显著降低磨损率，由室温下的 2.69×10^{-4} $mm^3 \cdot (N \cdot m)^{-1}$ 显著降低至 6.90×10^{-7} $mm^3 \cdot (N \cdot m)^{-1}$。该结果表明通过增材制造可以制备具有优异高温耐磨性的难熔高熵合金，也为开发能够承受极端条件的功能涂层开辟了道路。

Figures

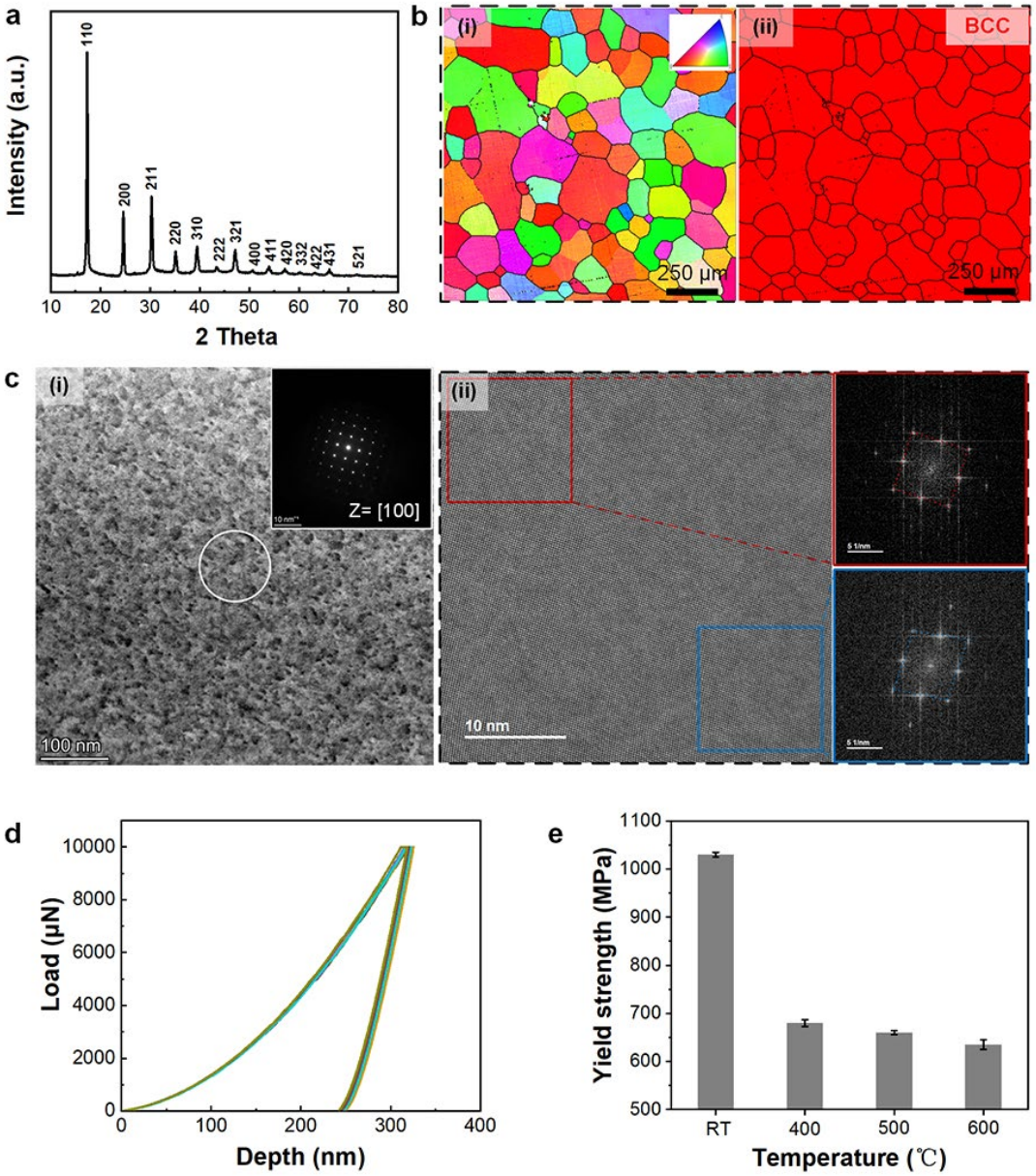

Fig. 1 The microstructure and properties of LENS-fabricated T42 alloy. **a** XRD profile showing the presence of a single BCC structure. **b** (i) IPF and (ii) phase figures. **c** (i) bright field picture with inserted SAED pattern collected from the marked area along zone axis of [1 0 0]; (ii) atomic structure with corresponding FFT images showing the difference in the lattice structure in different areas. **d** Load vs depth curves from nano-indentation experiments. **e** Average tensile yield strength of fabricated T42 alloy as a function of temperatures.

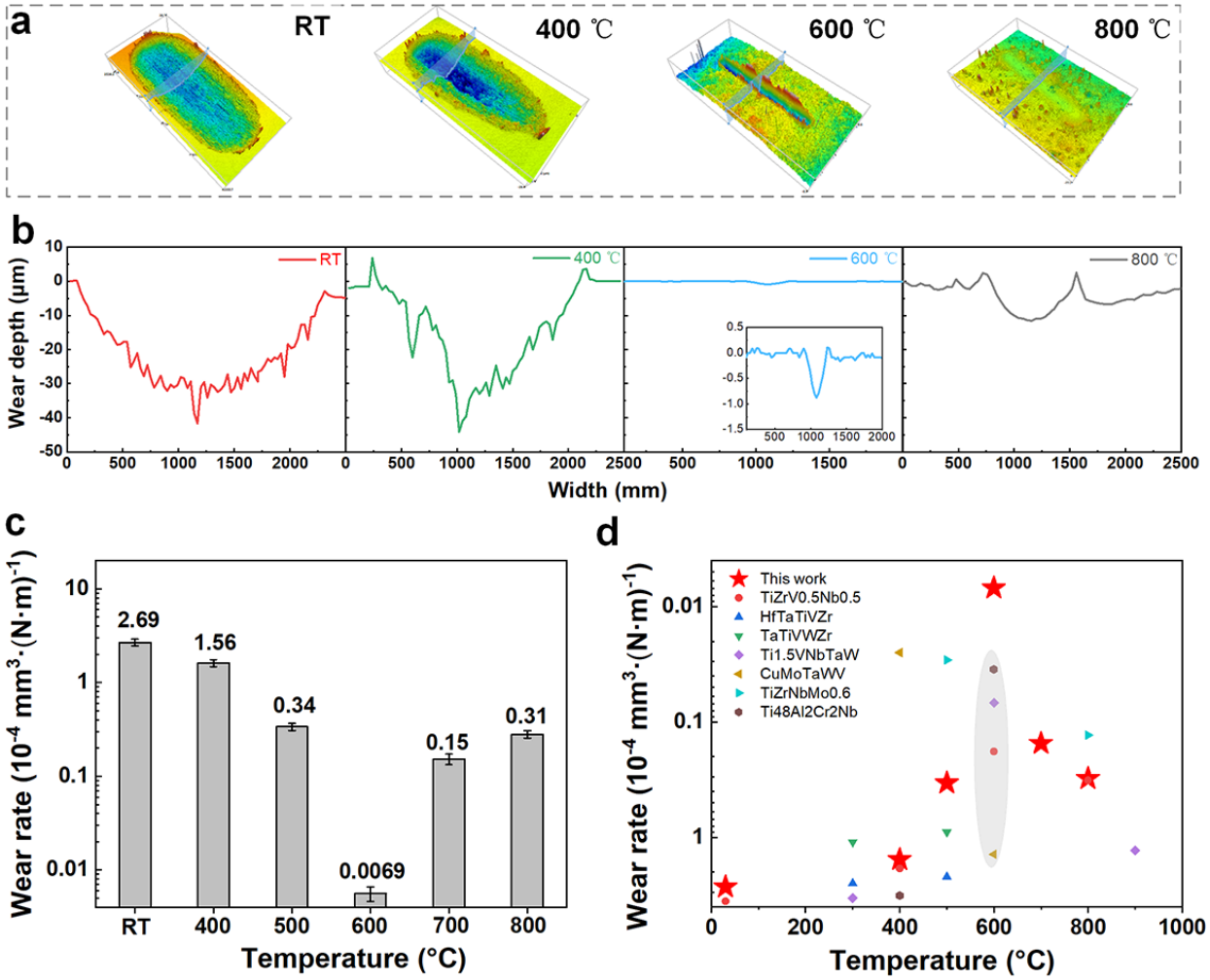

Fig. 2 **a** Worn scars of as-fabricated RHEA at various temperatures. **b** line profiles of the cross-section from the corresponding worn scars. **c** Wear rates of fabricated RHEA under different temperatures and **d** Comparison of wear rates between different HEAs [9,18–20,27,28].

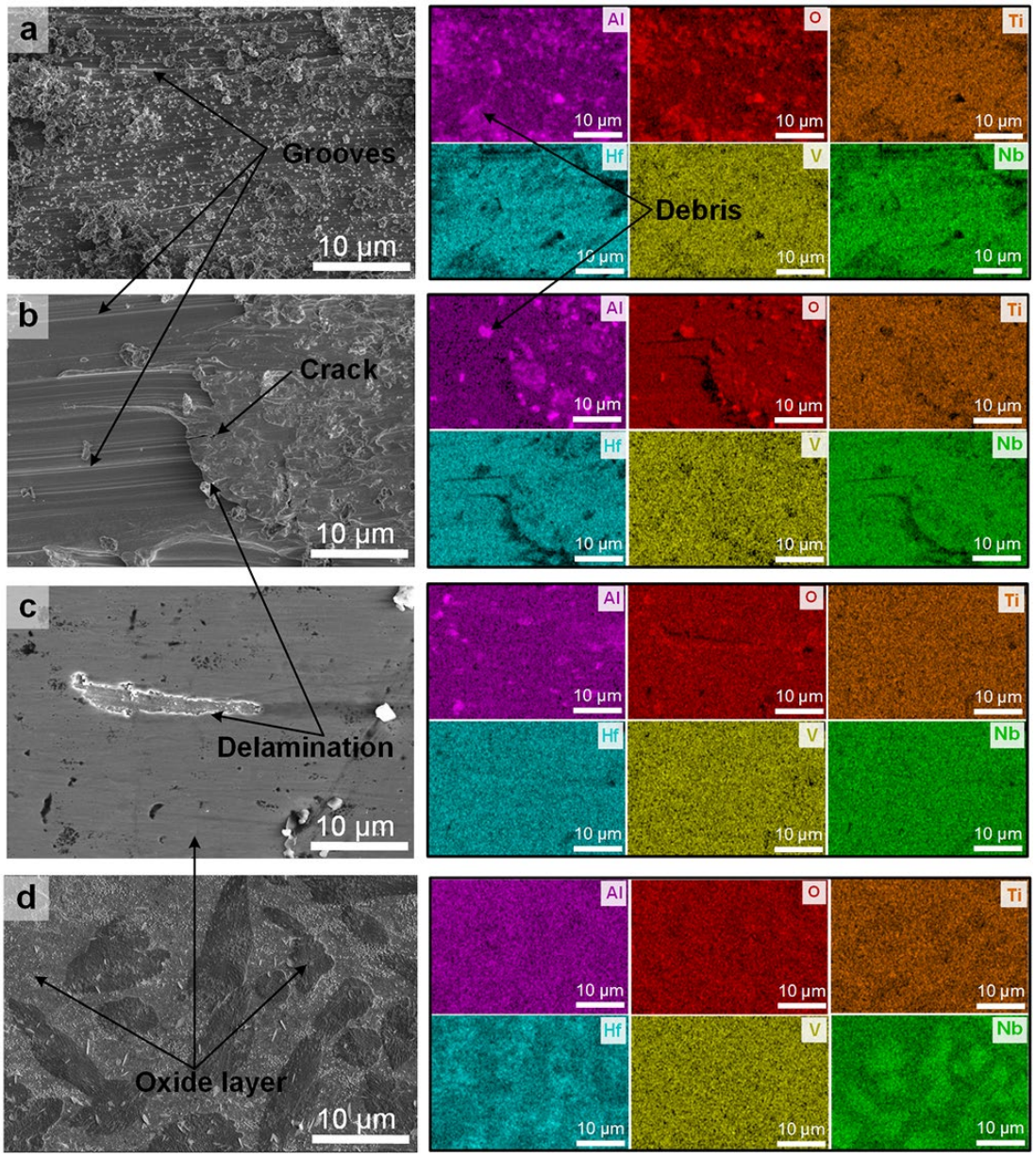

Fig. 3 Wear surface morphologies and corresponding EDS analysis of fabricated RHEAs after dry friction tests under different temperatures: **a** RT, **b** 400, **c** 600, and **d** 800 ℃.

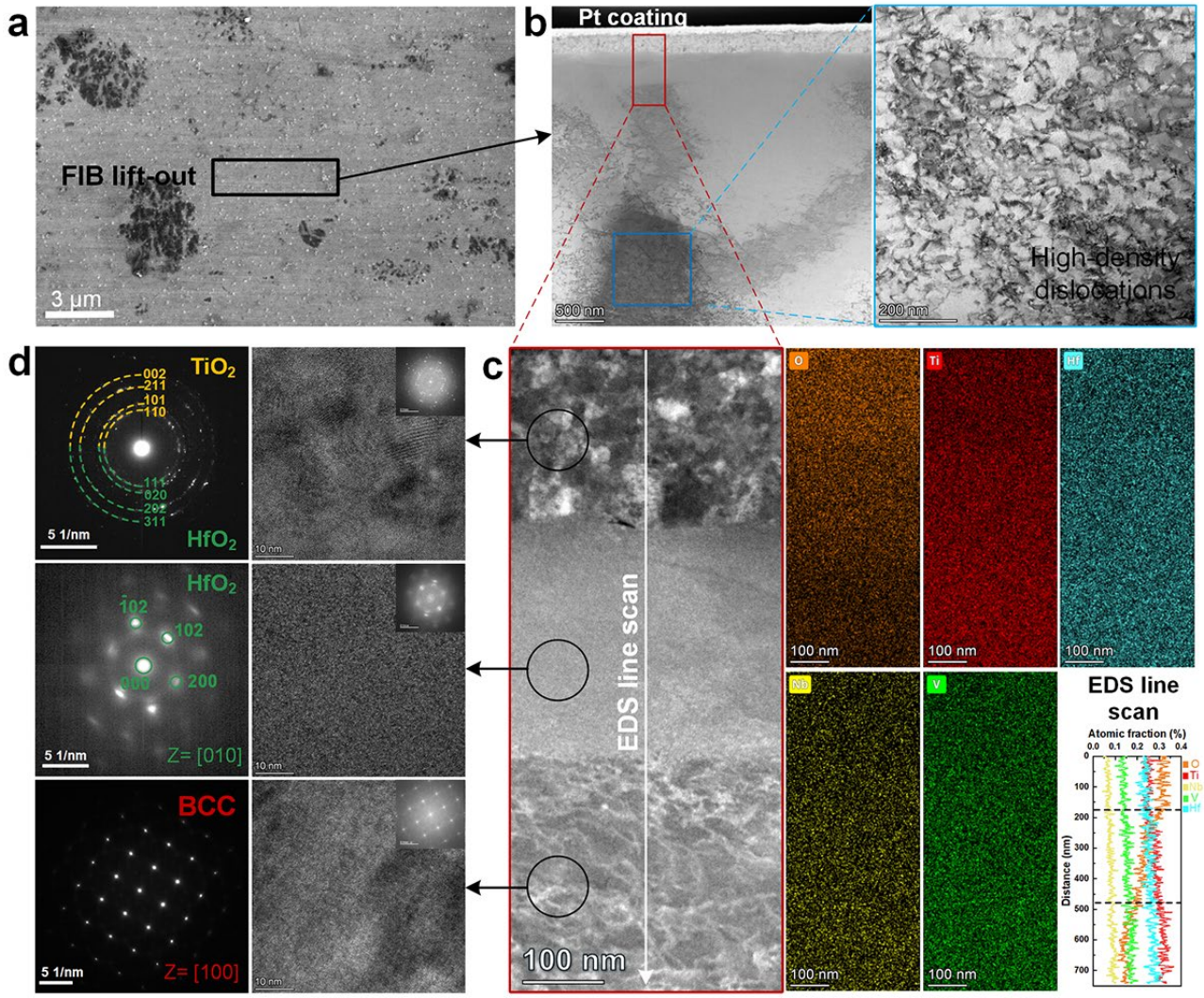

Fig. 4 Microstructure on the cross-section of wear scar after 600 ℃ friction test. **a** SEM image showing the TEM sampling area by FIB lift-out method. **b** TEM bright field image indicating the presence of layer structure and high density of dislocations. **c** The corresponding enlargement of marked area in **b** illustrating the obvious laminate structures and the elemental gradient on corresponding elemental distribution images. **d** The SAED patterns and HRTEM images from different layers beneath the wear scar, giving the presence of various metallic compounds.

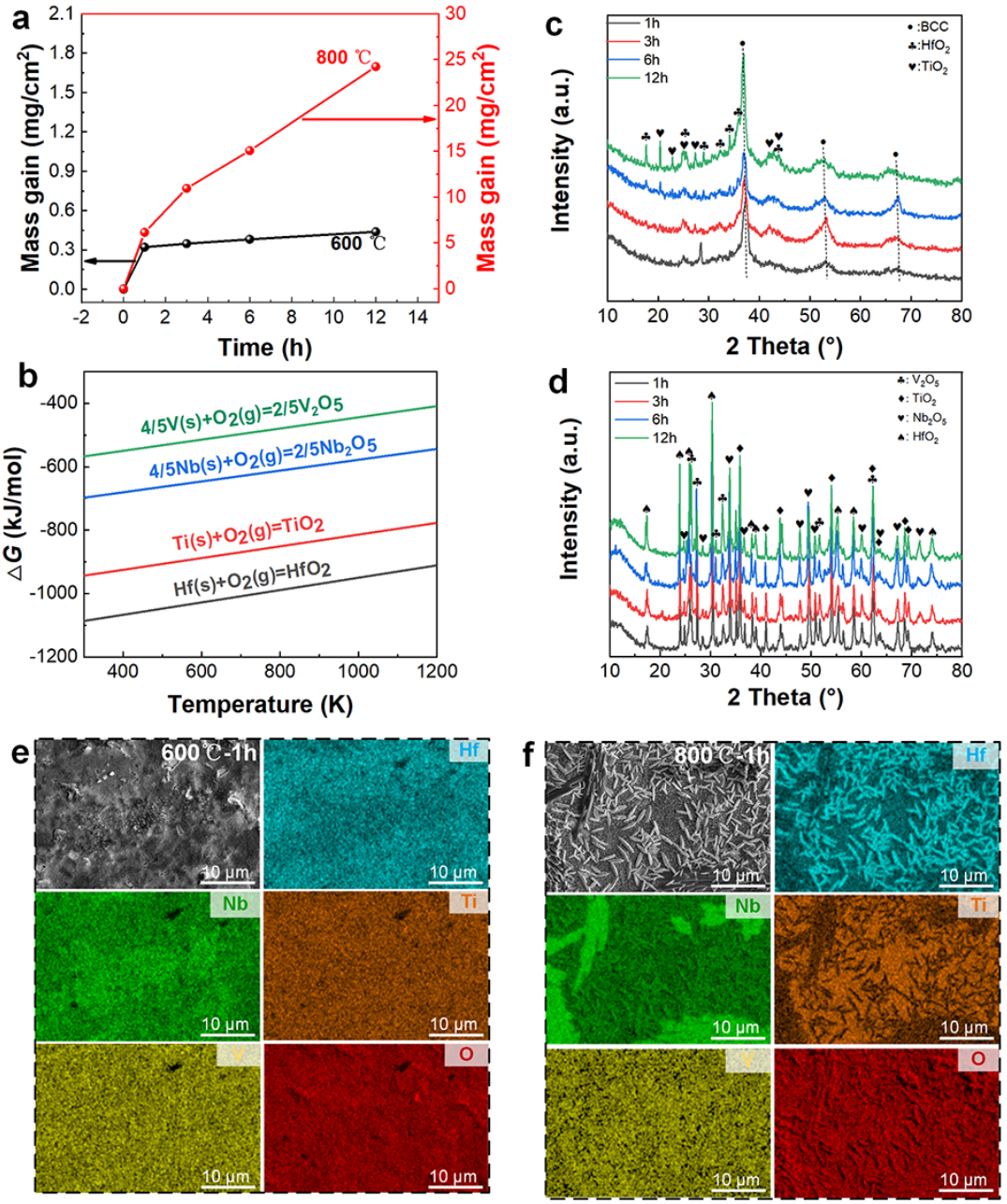

Fig. 5 Oxidation experimental results of the fabricated RHEA at 600 and 800 ℃. **a** The mass gain as a function of processing time. **b** The Gibbs free energy of oxidation reactions of the alloying constituents in the fabricated alloy. XRD patterns of the samples oxidized after **c** 600 and **d** 800 ℃. Oxidation morphologies with corresponding EDS maps of fabricated RHEA at **e** 600 and **f** 800 ℃ for 1 h.

TOC (Table of Content)